Korean Journal of Chemical Engineering (2024) 41:375–383
https://doi.org/10.1007/s11814-024-00103-7

REVIEW ARTICLE (INVITED ONLY)

Overview of Highly Solvating Electrolytes for Lean Electrolyte Conditions in Lithium–Sulfur Batteries

Taemin Kang[1] · Naehyun Kang[1] · Jang Wook Choi[1]

Received: 4 June 2023 / Revised: 20 September 2023 / Accepted: 4 October 2023 / Published online: 16 February 2024

Abstract

Lithium-sulfur (Li–S) batteries are considered the next generation of lithium-ion batteries due to their high energy density, but they face challenges in operation under lean electrolyte conditions. Among the potential strategies, highly solvating electrolytes (HSEs) have become a prominent option. These electrolytes offer strong solvation of polysulfide intermediates, leading to modified sulfur reaction pathways and deposition morphologies compared to conventional electrolytes. This review presents a comprehensive summary of HSEs in Li–S batteries, with a focus on their development and optimization for broad applications.

Keywords Lithium–sulfur batteries · Lean electrolyte condition · Lithium polysulfide solubility · Trisulfur radical anion · Li_2S deposition morphology

Introduction

In the past decade, the extensive utilization of lithium-ion batteries (LIBs) has significantly advanced technology in areas such as electric vehicles, portable electronics, and grid-scale energy storage systems (ESSs) [1–6]. However, the limitations of the Li^+ insertion/extraction chemistry have led LIBs to approach their energy density limits of 250 Wh kg^{-1} [7–13]. This restriction hinders their ability to meet the growing demand for high power and extended range in emerging applications. As a result, there is an increasing interest in exploring alternative energy storage systems that can surpass the performance of conventional LIBs.

Lithium-sulfur (Li–S) batteries have been gaining prominence as one of the most promising alternatives to conventional LIBs, primarily due to their high theoretical energy density of 2510 Wh kg^{-1} (or 2800 Wh L^{-1}) [14, 15]. They utilize elemental sulfur as the cathode, which is abundant, cost-effective, and environmentally friendly [16–23]. Despite these favorable characteristics, realizing the full potential of Li–S batteries remains a complex and ongoing challenge [24–30].

The maximum potential of Li–S batteries can be achieved by fully utilizing the active material, which entails the conversion of elemental sulfur (S_8) to lithium sulfide (Li_2S) and vice versa. Nevertheless, several factors impede the full utilization of sulfur, including the insulating properties of S_8 and Li_2S, the complex conversion reactions involving various dissoluble lithium polysulfide (LiPS) intermediates, and the shuttle effect that occurs between the cathode and anode [31–38]. Additionally, sulfur utilization is heavily dependent on the electrolyte quantity, as the reaction between sulfur and lithium is a distinctive solid–liquid-solid conversion process [27, 39].

Numerous studies have evaluated the performance of sulfur electrodes under high electrolyte-to-sulfur (E/S) ratio conditions, typically exceeding 10 μL mg_{sulfur}^{-1}, to achieve high specific capacities [40]. However, using a large amount of electrolytes comes at the expense of energy density. Even with a low E/S ratio of 3 μL mg_{sulfur}^{-1}, the electrolyte mass accounts for approximately 47.5% of the cell's total weight, far above the typical values of conventional LIBs [41]. Although minimizing the E/S ratio can enhance energy density, it can also give rise to problems such as low ionic conductivity, sluggish reaction kinetics, and ultimately, poor cycle life. Therefore, it is crucial to explore electrolytes that can function effectively

Taemin Kang and Naehyun Kang contributed equally.

✉ Jang Wook Choi
jangwookchoi@snu.ac.kr

[1] School of Chemical and Biological Engineering and Institute of Chemical Processes, Seoul National University, 1 Gwanak-ro, Gwanak-gu, Seoul 08826, Republic of Korea

in lean conditions while simultaneously addressing these problems.

Among the electrolytes, 1,3-dioxolane/1,2-dimethoxyethane (DOL/DME) has been widely used due to its superior ability to form a stable interface with lithium metal anodes (LMAs). However, DOL/DME encounters challenges when employed with a low E/S ratio in Li–S battery cells. Reduced E/S ratio impedes the dissolution of long-chain polysulfides, consequently diminishing reaction kinetics. To deal with this issue, the concept of highly solvating electrolytes (HSEs) has been introduced. These electrolytes, such as *N,N*-dimethylacetamide (DMA) and dimethyl sulfoxide (DMSO), with a high Gutmann donor number (DN), have enhanced solubility to long-chain polysulfides [27, 42–45]. As a result, improved reaction kinetics and sulfur utilization can be achieved even under low E/S ratio [24, 26, 27]. However, these advantages come with a trade-off, as the intensified shuttle effect leads to compatibility issues with LMAs, ultimately affecting the battery's cycle life.

The objective of this review is to provide a comprehensive overview of the current state of research on HSEs in Li–S batteries. Our investigation will address the radical-containing reaction mechanism and the form of Li_2S deposition due to the high solvation power of HSEs. It will also include the challenges faced by HSEs and introduce potential strategies to overcome these obstacles. Our goal is to provide scientific insights that will contribute to the development of high-performance Li–S batteries and pave the way for further advances in the field of energy storage.

Highly Solvating Electrolytes

As previously mentioned, HSEs are being treated as prospective solutions to increase the energy density of Li–S batteries. Enhanced LiPS solubility in HSEs is attributed to the formation of trisulfur radical anions ($S_3^{\bullet-}$) which creates a new reaction pathway that facilitates the conversion reaction, leading to significantly improved sulfur utilization and reduced E/S ratio. Additionally, the use of HSEs can effectively mitigate the passivation of the electrode by Li_2S, an insulating material. Generally, solid-state Li_2S is formed at the end of the conversion and passivates the electrode surface of the active materials. However, HSEs have high solvating power to increase the nucleation overpotential of Li_2S inducing slow 3D deposition to expose fresh surfaces. This enables HSEs to both prevent passivation and maintain battery performance over multiple cycles.

Enhancing LiPS Solubility for Improved Performance in Li–S Batteries

LiPS is a crucial component in the electrochemical operation of Li–S batteries. During discharge, sulfur in the cathode reacts with lithium ions, forming soluble LiPSs with various chain lengths that can readily transfer between the cathode and anode through the electrolyte. The soluble nature of LiPSs leads to their accumulation at the cathode-electrolyte interface, thereby facilitating their conversion and improving reaction kinetics. However, their low solubility in most electrolytes limits the utilization of active materials in the cathode, demanding an excess amount of electrolyte in a cell. To address this, researchers have investigated the use of HSEs with strong Lewis basicity to coordinate with Li^+ and further increase the solubility of LiPSs. This approach improves sulfur utilization and thus the volumetric energy density.

Comparing the performance of HSEs with conventional electrolyte, Pan et al. [44] conducted LiPS solubility tests for different types of electrolytes. Their results showed that DMSO with a high dielectric constant (ε) of 46.5 had a saturation solubility of 6 *M* for Li_2S_6, which was 6 times higher than that of DOL/DME (Fig. 1a). According to Gupta et al. [45], such low LiPS solubility of DOL/DME is not suitable for achieving low E/S ratio under practical conditions. They correlated LiPS solubility with the E/S ratio based on a cell level with 75 wt% sulfur content in the cathode (Fig. 1b, c). Theoretically, the E/S ratio of 5 μL mg_{sulfur}^{-1} corresponds to 1 *M* Li_2S_6, while practically, the E/S ratio of 2 μL mg_{sulfur}^{-1} corresponds to 1.6 *M* Li_2S_6. As shown in Fig. 1d, all polysulfides were clearly soluble in high DN solvents (DMA, DMSO, and 1-Methylimidazole (MeIm)), whereas DOL/DME, which has a relatively low DN, displayed an obvious precipitation, reflecting its incapability to accommodate high polysulfide concentrations. Zhang et al. [46] reported a cosolvent of high-ε tetramethylurea (TMU) and DOL in a 1:1 volume ratio, which can dissolve Li_2S_4 and Li_2S_8 up to 1.3 *M* and 1 *M*, respectively (Fig. 1e). DOL/TMU demonstrated the highest reversible capacity (approximately 500 mAh g^{-1}) with a stable average Coulombic efficiency of 99.6% during 180 cycles at the cell level (Fig. 1f). Furthermore, the pouch cell exhibited high sulfur utilization of 91.0% and high energy density of 324 Wh kg^{-1} (Fig. 1g). Cheng et al. [47] developed a new eutectic solvent composed of ε-caprolactam (CPL) and acetamide in a 1:1 molar ratio to dissolve a maximum of 0.7 *M* Li_2S_x (where $x = 1, 2, 4, 6, 8$), respectively (Fig. 1h). The solvent exhibited considerable solubility of LiPSs even after being mixed with a 1:1 volume ratio of DOL/DME (Fig. 1i). Baek et al. [26] identified a novel high DN solvent, known as 1,3-dimethyl-2-imidazolidinone (DMI), that has the ability to solvate 1.5 *M* Li_2S_6. In contrast, DOL/DME and ethylene carbonate/dimethyl carbonate (EC/DMC) demonstrated limited solvation capacity, resulting in the precipitation of Li_2S_6 instead of dissolution (Fig. 1j).

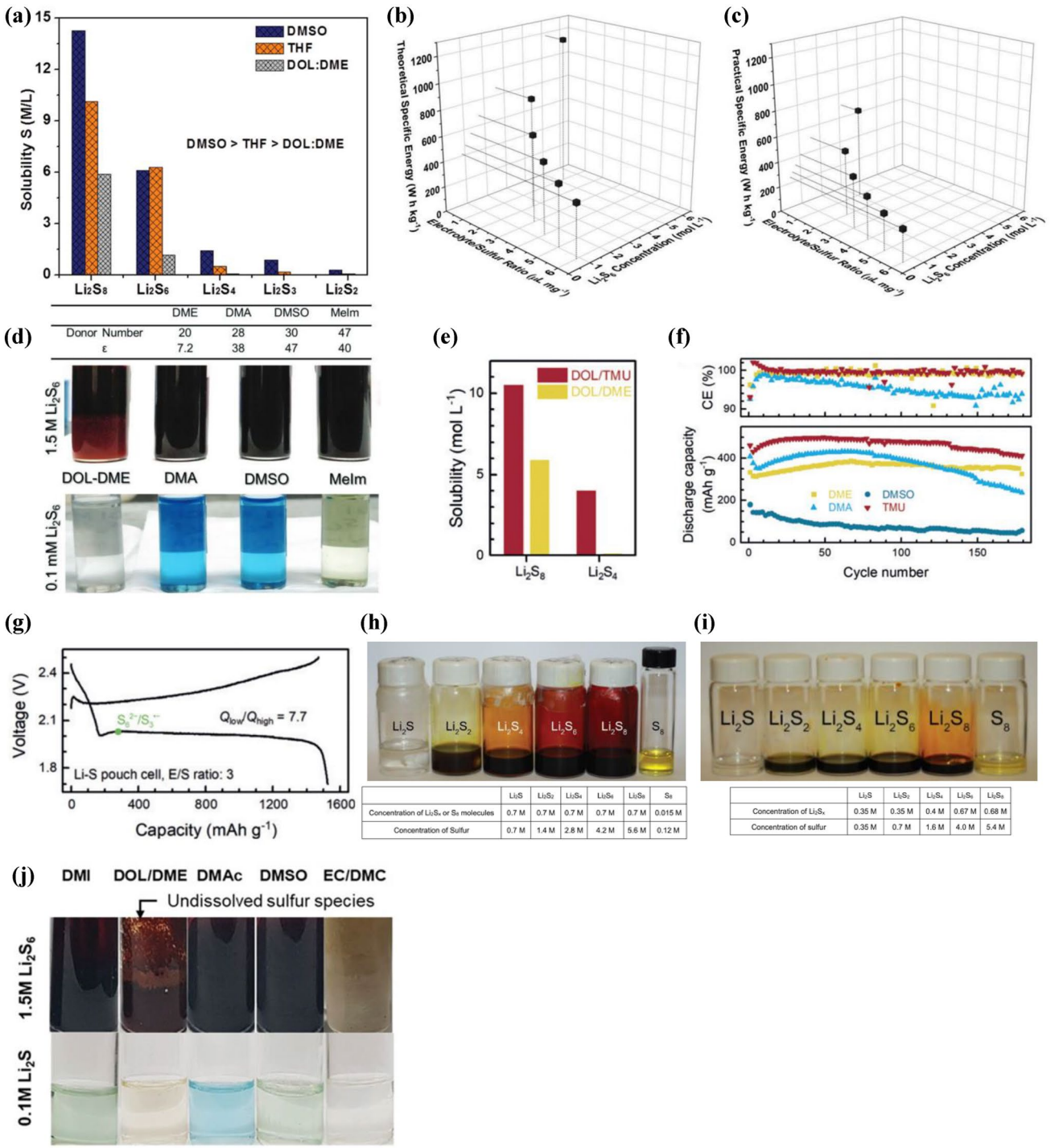

Fig. 1 **a** LiPS solubility test for DMSO, THF (Tetrahydrofuran), DOL/DME. Reproduced with permission [44]. Copyright 2015, Wiley–VCH. E/S ratio and Li_2S_6 concentration in relation to **b** theoretical specific energy (assumed a capacity as 1672 mAh g^{-1}) **c** practical specific energy (assumed a capacity as 1000 mAh g^{-1}). **d** Optical images of 1.5 *M* Li_2S_6 solubility tests for DOL/DME, DMA, DMSO, and MeIm along with DN and dielectric constant. Reproduced with permission [45]. Copyright 2019, Wiley–VCH. **e** Solubility of Li_2S_8 and Li_2S_4 in DOL/TMU and DOL/DME. **f** Cycling performance of Lilpolysulfide cells using carbon paper as cathode current collectors at a current density of 0.1 C. **g** The galvanostatic curve of the initial cycle of a pouch cell with TMU electrolyte (S loading: 2.5 mg cm^{-2}). Reproduced with permission [46]. Copyright 2018, Wiley–VCH. Optical images of solubility test for **h** the eutectic solvents and **i** the eutectic solvents/DOL/DME (2:1:1 vol%) with saturated Li_2S_x (where $x = 1, 2, 4, 6, 8$). Reproduced with permission [47]. Copyright 2019, Wiley–VCH. **j** Optical images of (top) 1.5 *M* Li_2S_6 in DMI, DOL/DME, DMA, DMSO, and EC/DMC, and (bottom) 0.1 *M* Li_2S in the same solvents. Reproduced with permission [26]. Copyright 2020, Wiley–VCH

Influence of Electrolyte Properties on the Conversion Reaction Mechanisms of Sulfur

HSEs exhibit a unique disproportionation and dissociation behavior associated with blue radical species ($S_3^{\bullet-}$) [48], which have been detected through Ultraviolet–visible (UV–vis) spectroscopy [48–50] and electron spin resonance measurements [48, 50]. Depending on the presence of these species, they significantly influence the electrochemical characteristics of HSEs compared to DOL/DME.

(i) DOL/DME

Lu et al. [51] conducted rotating ring disk electrode (RRDE) studies, which confirmed that S_8^{2-} is generated initially through the two-electron reduction of S_8 (Eq. 1), as previously proposed in the literature [42, 49–56].

$$S_8 + 2e^- \rightarrow S_8^{2-} \tag{1}$$

$$S_8^{2-} + 2e^- \rightarrow 2S_4^{2-} \tag{2}$$

The generation of solid-state species during the sulfur reduction in DOL/DME was suggested by previous studies such as RRDE [51] and *operando* X-ray absorption spectroscopy (XAS) [57].

$$S_4^{2-} + 2e^- \rightarrow 2S_2^{2-} \tag{3}$$

(ii) HSEs

Unlike in DOL/DME, the reduction of S_8^{2-} produces both S_6^{2-} and S_8, as reflected in the UV spectra by an increase of the S_6^{2-} signal (Eq. 4) [16, 43, 56, 58–61].

$$S_8^{2-} \rightarrow S_6^{2-} + \frac{1}{4}S_8 \tag{4}$$

The subsequent increase of the $S_3^{\bullet-}$ signal is characterized by the dissociation of S_6^{2-} (Eq. 5) [16, 43, 56, 58–61].

$$S_6^{2-} \rightarrow 2S_3^{\cdot-} \tag{5}$$

Through the second plateau in the discharging process, $S_3^{\bullet-}$ undergoes further reduction, leading to S_3^{2-} and S_4^{2-} (Eqs. 6, 7) [42, 43, 62, 63]. S_4^{2-} and $S_3^{\bullet-}$ react with S_8 to facilitate the abundant utilization of sulfur sources [16, 42, 43, 58–63].

$$S_3^{\cdot-} + e^- \rightarrow S_3^{2-} \tag{6}$$

$$S_3^{2-} + 2S_3^{\cdot-} \rightarrow 3S_4^{2-} \tag{7}$$

$$S_4^{2-} + \frac{1}{4}S_8 \rightarrow 2S_3^{\cdot-} \tag{8}$$

$$2S_3^{\cdot-} + \frac{1}{4}S_8 \rightarrow S_8^{2-} \tag{9}$$

Finally, when it comes to the depletion of S_8^{2-} and $S_3^{\bullet-}$, Li_2S is formed as a final product.

$$S_4^{2-} + 6e^- \rightarrow 4S^{2-} \tag{10}$$

Cuisinier et al. [42] implemented X-ray absorption near edge structure (XANES) to investigate the conversion mechanisms of sulfur in HSEs, specifically DMA. The study revealed that sulfur was fully consumed by $S_3^{\bullet-}$ during discharge, as indicated by the simultaneous disappearance of elemental sulfur and $S_3^{\bullet-}$ (Fig. 2a). Using linear combination fitting (LCF) analysis of XANES spectra (Fig. 2b), they were able to distinguish the $S_3^{\bullet-}$ peak (2468.5 eV) from that of S_n^{2-} (2470.5 eV, $n = 4, 6, 8$) and elucidate the significant fraction of S_4^{2-} in the second step of discharge (Eq. 7). These results were consistent with the galvanostatic curve of the initial cycle, which showed 94% utilization of sulfur (Fig. 2c). Zou and Lu [63] conducted an *operando* UV–vis spectroscopy analysis in both DOL/DME and DMSO to verify the stability of intermediate sulfur species (Fig. 2d–g). They found that stable intermediates in DOL/DME were limited to only S_4^{2-} species, while DMSO facilitated multiple reaction pathways through $S_3^{\bullet-}$. They were able to demonstrate the disproportionation of S_8^{2-} and dissociation of S_6^{2-} (Eqs. 4, 5). Additional UV–vis spectra of *N,N*-dimethylformamide (DMF) showed lower S_n^{2-} peaks but a higher $S_3^{\bullet-}$ peak (at 617 nm) than DMSO, which suggests that $S_3^{\bullet-}$ is more stable in DMF, resulting in reduced electrochemical polarization (Fig. 2h, i). The effectiveness of DMI, a new high DN solvent, in stabilizing $S_3^{\bullet-}$ has been substantiated by optical images of 0.1 *M* Li_2S in the solvent and UV–vis absorption spectra of 1 *mM* Li_2S_6 in the solvent [26].

Impact of Solvent Dynamics on the Morphology of Li_2S Deposition

The reaction between sulfur and lithium generates soluble polysulfides with various chain lengths, eventually leading to the insoluble Li_2S. However, the low ionic conductivity of Li_2S affects the growth pattern and reversibility of charge and discharge processes. Due to the conductivity limitations, Fan et al. [64] discovered that Li_2S growth in the thickness direction through bulk diffusion is not favored. By means of a potentiostatic experiment, they proposed that the lateral growth of Li_2S is attributed to

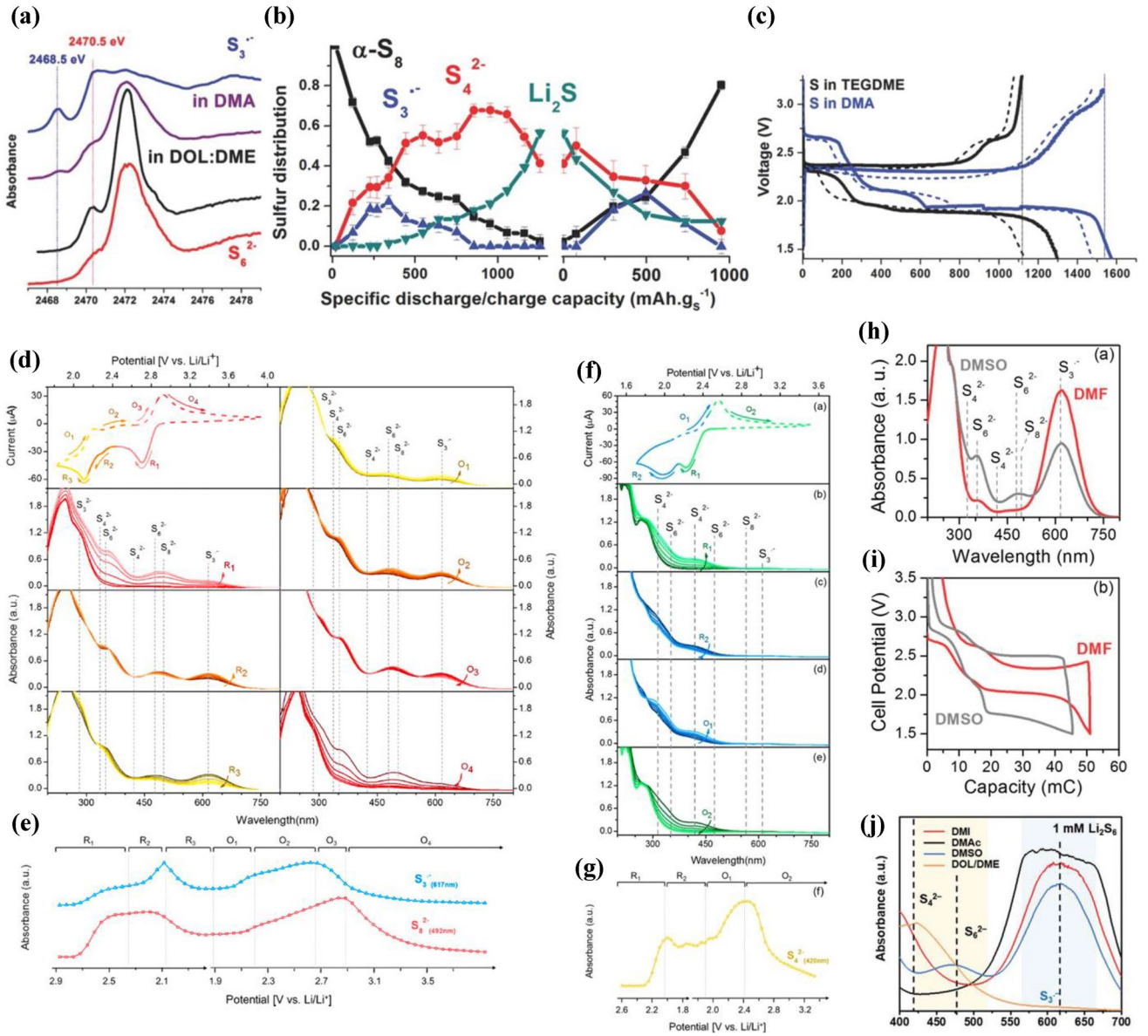

Fig. 2 **a** Sulfur K-edge XANES during discharge (around 340 mAh g^{-1}) in Li–S cells using DMA and DOL/DME electrolytes compared with $S_3^{\bullet-}$ and S_6^{2-} reference materials. **b** LCF analysis of the XANES spectra. **c** The galvanostatic curves of sulfur in tetraethylene glycol dimethyl ether (TEGDME) and DMA electrolytes at 0.1 C. (Solid: first cycle, dotted: second cycle) Reproduced with permission [42]. Copyright 2015, Wiley–VCH. **d** Cyclic voltammetry (CV) of 2.0 *mM* S_8 and 1.0 *M* Lithium bis(trifluoromethanesulfonyl)imide (LiTFSI) in DMSO (top left) and *operando* UV – vis spectra for each reaction step throughout the CV scan. **e** UV – vis absorbance at 617 and 492 nm during the CV. **f** CV of 2.0 *mM* S_8 and 1.0 *M* LiTFSI in DOL/DME (top) and *operando* UV – vis spectra for each reaction step throughout the CV scan. **g** UV – vis absorbance at 420 nm during the CV. **h** UV – vis absorption spectra of 2.0 *mM* S_6^{2-} in DMSO and DMF. **i** Galvanostatic curves of 4.0 *mM* S_8 and 1.0 *M* LiTFSI in DMSO and DMF at 1 C. Reproduced with permission [63]. Copyright 2015, American Chemical Society. **j** UV – vis absorption spectra of 1.0 *mM* of Li_2S_6 in DMI, DMA, DMSO, DOL/DME. Reproduced with permission [26]. Copyright 2020, Wiley–VCH

the reduction of polysulfides in solution at the three-phase boundary between Li_2S precipitates, a substrate, and the solution (Fig. 3a, b). Furthermore, they conducted a comparative study of discharge currents at C/4 and C/24 to explore the relationship between discharge rate and Li_2S morphology (Fig. 3c, d). The study indicated that particle growth dominates at slow discharge rates, while nucleation dominates at higher rates.

To confirm the impact of DN on the Li_2S deposition pattern, Pan et al. [65] presented scanning electron microscope (SEM) images of the morphologies of Li_2S after discharging in solvents with different DN (Fig. 3e, f). They

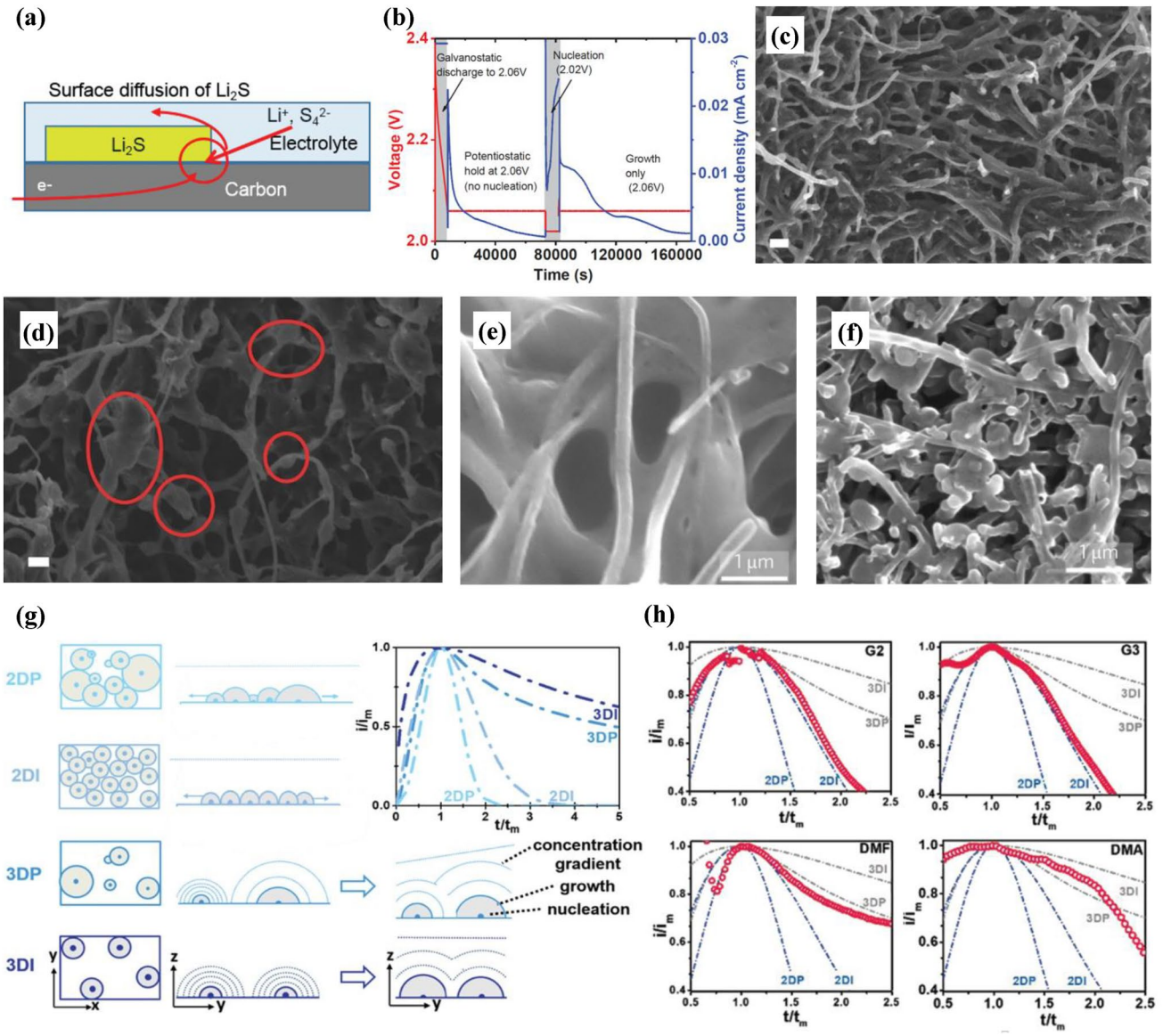

Fig. 3 **a** Schematic image of the mechanism for the lateral growth of Li_2S. **b** Potentiostatic experiment. SEM images of polysulfide solution-multi-walled carbon nanotube (MWCNT) cathodes discharged **c** at C/4 and **d** C/24. Scale bars are 200 nm. Reproduced with permission [64]. Copyright 2015, Wiley–VCH. SEM images of Li_2S morphologies discharged **e** in TMS **f** in DMSO. Reproduced with permission [65]. Copyright 2017, Springer Nature. **g** Schematic illustration of 2DP/2DI (Bewick, Fleischman, and Thirsk (BFT) models) and 3DP/3DI (Scharifker–Hills (SH) models). **h** Chronoamperograms of Li_2S deposition in various electrolytes. (i_m: peak current; t_m: time needed to achieve the peak current) Reproduced with permission [66]. Copyright 2019, Wiley–VCH

observed that the low DN solvent, tetramethylene sulfone (TMS) resulted in a 2D film-shaped morphology, whereas the high DN solvent, DMSO produced a 3D particle-shaped morphology. Similarly, Li et al. [66] investigated the kinetics of Li_2S deposition in solvents with varying DN by analyzing current–time transient curves from chronoamperic tests using four classical models of the electrochemical deposition (Fig. 3g). They elucidated that the behavior of low DN glymes could be explained by a 2D nucleation model, indicating that diffusion predominantly occurs along the surface. On the other hand, high DN solvents facilitated more solvated Li_2S diffusion in the solution before it precipitated onto the Li_2S clusters, following a 3D nucleation model (Fig. 3h). Choi's group [24, 26, 27] noted a significant difference in Li_2S morphologies in two distinct types of electrolytes: DOL/DME and HSEs. In DOL/DME, the insulating Li_2S grew laterally, resulting in surface passivation. Conversely, HSEs exhibited high nucleation overpotential followed by low nucleation

Table 1 Summary of the electrochemical performances in Li–S batteries

Electrolyte	Areal sulfur loading (mg cm^{-2})	Initial capacity (mAh g^{-1}) @ C-rate	Cycle number @ C-rate	Capacity retention (%)	E/S ratio (μL mg_{sulfur}^{-1})	References
1 *M* LiTFSI 0.2 *M* $LiNO_3$ DOL/DME (1:1 vol%)	1	1150 @ 0.03 C	40 cycles @ 0.1 C	N/A	5	[26]
2 *M* $LiNO_3$ DMA	1.5	1530 @ 0.1 C	20 cycles @ 0.1 C	62	50	[42]
1 *M* LiTFSI 0.4 *M* $LiNO_3$ DMSO	N/A	230 @ 0.05 C	N/A	N/A	8.8	[66]
1 *M* LiTFSI 0.4 *M* $LiNO_3$ MeIm	N/A	356 @ 0.05 C	N/A	N/A	8.8	[66]
1 *M* LiTFSI 0.3 *M* $LiNO_3$ DOL/TMU (1:1 vol%)	2.5	1134 @ 0.1 C	20 cycles @ 0.1 C	N/A	N/A	[46]
1 *M* LiTFSI 0.5 *M* $LiNO_3$ DMI	1	1225 @ 0.03 C	80 cycles @ 0.1 C	59.6	5	[26]
1 *M* LiTFSI 0.4 *M* $LiNO_3$ DMF	N/ A	819 @ 0.05 C	N/A	N/A	8.8	[66]
1 *M* LiTFSI 3-FPN	1	1087.9 @ 0.03 C	100 cycles @ 0.1 C	72.6	7	[24]
0.2 *M* Li_2S_8 1 *M* LiBr 0.2 *M* $LiNO_3$ DOL/DME (1:1 vol%)	N/A	1535 @ 0.1 C	80 cycles @ 0.2 C	N/A	19.5	[67]
0.2 *M* Li_2S_8 1 *M* LiTf 0.2 *M* $LiNO_3$ DOL/DME (1:1 vol%)	N/A	1214 @ 0.1 C	80 cycles @ 0.2 C	N/A	19.5	[67]
0.4 *M* LiTFSI 0.6 *M* $LiNO_3$ DOL/DME (1:1 vol%)	3	1200 @ 0.1 C	100 cycles @ 0.1 C	88.7	5	[68]
0.2 *M* LiTFSI 0.2 *M* $LiNO_3$ 0.8 *M* LiSCN DOL/DME (1:1 vol%)	3	1365.8 @ 0.2 C/0.1 C	80 cycles @ 0.2 C/0.1 C	N/A	5	[69]
1 *M* LiTFSI TEGDME	N/A	730 @ 0.01 C	N/A	N/A	N/A	[70]

density, thereby exposing a substantial surface area of the electrode with 3D particle-shaped Li_2S deposition.

In short, the solvents with high DN effectively stabilize long-chain polysulfides, leading to a deceleration of the nucleation process [66]. Subsequently, a reduced density of nuclei results in 3D morphology of Li_2S on the cathode surface and a great portion of the electrode surface remains exposed for fresh reaction [24, 26, 27, 65–69]. On the contrary, low DN solvents tend to show a rapid nucleation process, resulting in the formation of film-like insulating layer to passivate the cathode surface. Furthermore, in addition to these advantages, high DN solvents that possess Li_2S solubility promote the reversible reaction of sulfur.

Conclusion and Future Outlook

Li – S batteries have emerged as a promising candidate for post-lithium-ion batteries owing to the high gravimetric capacity of elemental sulfur (1675 mAh g^{-1}). To achieve the highest energy density by fully utilizing the capacity of sulfur, it is necessary to operate under lean electrolyte conditions. HSEs can facilitate this by enhancing the solubility of LiPSs mediated by the $S_3^{\bullet-}$, leading to higher specific capacity and energy density even under low E/S ratio (Table 1). Also, HSEs provide a 3D deposition morphology of Li_2S, ensuring a sufficient electrode surface to maintain the redox reaction without passivation.

While the application of HSEs represents an effective strategy to enhance kinetics and achieve high energy density in Li–S batteries, they also pose challenges such as the shuttle effect, which can lead to a detrimental reaction with the Li anode. Furthermore, the decrease in the E/S ratio increases the LiPS concentration, resulting in sacrificed ionic conductivity and expanded voltage hysteresis. This reduces sulfur utilization and energy efficiency, hindering the practical application of lean-electrolyte Li–S batteries.

To overcome these challenges, several strategies have been explored, including electrolyte engineering, artificial solid electrolyte interphase (SEI) layers formation, membrane modification, and the addition of excess Li-salts. In recent years, several studies have demonstrated remarkable approaches to stabilize Li-metal electrodes while maintaining LiPS solubility. As an example, in one study, 3-fluoropyridine (3-FPN), a dual functional high DN solvent with significant polysulfide solubility, was utilized to form LiF-rich SEI, resulting in enhanced cycling properties [24]. Additionally, other investigations modified the Li^+ solvation structure to induce the 3D deposition of Li_2S [67] and generate Li_3N-rich SEI layers [68, 69] by using high DN salt anions (LiBr, $LiNO_3$, LiSCN) in ether-based solvents. Both of these strategies formulate the stable SEI layers on lithium metal interfaces, leading to improved Li reversibility.

Further development of Li–S batteries utilizing HSEs requires a comprehensive approach. Optimization of electrolyte design is necessary to achieve an appropriate balance between polysulfide solubility and compatibility with LMAs. Additionally, it is essential to rationally design a sulfur cathode that effectively suppresses the formation and diffusion of LiPSs at the cathode. Moreover, an in-depth understanding of the electrochemical reaction mechanism of HSEs using advanced analytical methods is imperative.

Acknowledgements We acknowledge the support from the National Research Foundation of Korea (NRF) (NRF-2021M3H4A3A02086210), the Technology Innovation Program (20012341) funded by the Ministry of Trade, Industry & Energy (MOTIE) of Korea, and generous support from the Institute of Engineering Research (IOER) and Research Institute of Advanced Materials (RIAM) at Seoul National University.

Funding Open Access funding enabled and organized by Seoul National University. This article is funded by National Research Foundation of Korea, NRF-2021M3H4A3A02086210, Jang Wook Choi, Ministry of Trade, Industry and Energy, 20012341, Jang Wook Choi.

References

1. H. Park, D.H. Yeom, J. Kim, J.K. Lee, Korean J. Chem. Eng. **32**, 178 (2015)
2. H.S. Kang, P. Santhoshkumar, J.W. Park, G.S. Sim, M. Nanthagopal, C.W. Lee, Korean J. Chem. Eng. **37**, 1331 (2020)
3. N. Venugopal, W.S. Kim, T. Yu, Korean J. Chem. Eng. **33**, 1500 (2016)
4. M. Zhao, B.Q. Li, X.Q. Zhang, J.Q. Huang, Q. Zhang, ACS Cent. Sci. **6**, 1095 (2020)
5. Y.R. Liang, C.Z. Zhao, H. Yuan, Y. Chen, W.C. Zhang, J.Q. Huang, D.S. Yu, Y.L. Liu, M.M. Titirici, Y.L. Chueh, H.J. Yu, Q. Zhang, InfoMat **1**, 6 (2019)
6. X.W. Yu, A. Manthiram, Adv. Energy Sustain. Res. **2**, 2000102 (2021)
7. P.G. Bruce, S.A. Freunberger, L.J. Hardwick, J.-M. Tarascon, Nat. Mater. **11**, 19 (2012)
8. J.M. Tarascon, M. Armand, Nature **414**, 359 (2001)
9. H.S. Ko, H.W. Park, G.J. Kim, J.D. Lee, Korean J. Chem. Eng. **36**, 620 (2019)
10. Y. Li, Z.H. Li, C. Zhou, X.B. Liao, X.W. Liu, X.F. Hong, X. Xu, Y. Zhao, L.Q. Mai, Chem. Eng. J. **422**, 130107 (2021)
11. R. Saroha, J.H. Ahn, J.S. Cho, Korean J. Chem. Eng. **38**, 461 (2021)
12. V. Etacheri, R. Marom, R. Elazari, G. Salitra, D. Aurbach, Energy Environ. Sci. **4**, 3243 (2011)
13. H. Li, Joule **3**, 911 (2019)
14. J.W. Choi, D. Aurbach, Nat. Rev. Mater. **1**, 1 (2016)
15. L. Shi, F.L. Zeng, X. Cheng, K.H. Lam, W.K. Wang, A.B. Wang, Z.Q. Jin, F. Wu, Y.S. Yang, Chem. Eng. J. **334**, 305 (2018)
16. Y.X. Yin, S. Xin, Y.G. Guo, L.J. Wan, Angew. Chem. Int. Ed. **52**, 13186 (2013)
17. A. Manthiram, S.H. Chung, C. Zu, Adv. Mater. **27**, 1980 (2015)
18. R.J. Angelici, Acc. Chem. Res. **21**, 387 (1988)
19. Q. Pang, X. Liang, C.Y. Kwok, L.F. Nazar, Nat. Energy **1**, 1 (2016)
20. A. Manthiram, Y. Fu, S.H. Chung, C. Zu, Y.S. Su, Chem. Rev. **114**, 11751 (2014)
21. M. Rana, B. Luo, M.R. Kaiser, I. Gentle, R. Knibbe, J. Energy Chem. **42**, 195 (2020)
22. J. Xiang, Y. Zhao, L. Wang, C. Zha, J. Mater. Chem. A **10**, 10326 (2022)

23. S. Kim, W.G. Lim, A. Cho, J. Jeong, C. Jo, D. Kang, S.M. Han, J.W. Han, J. Lee, ACS Appl. Energy Mater. **3**, 2643 (2020)
24. A. Elabd, J. Kim, D. Sethio, S. Kang, T. Kang, J.W. Choi, A. Coskun, ACS Energy Lett. **7**, 2459 (2022)
25. J. Kim, H. Shin, D.J. Yoo, S. Kang, S.Y. Chung, K. Char, J.W. Choi, Adv. Funct. Mater. **31**, 2106679 (2021)
26. M. Baek, H. Shin, K. Char, J.W. Choi, Adv. Mater. **32**, e2005022 (2020)
27. H. Shin, M. Baek, A. Gupta, K. Char, A. Manthiram, J.W. Choi, Adv. Energy Mater. **10**, 2001456 (2020)
28. J. Kim, A. Elabd, S.Y. Chung, A. Coskun, J.W. Choi, Chem. Mater. **32**, 4185 (2020)
29. H. Shin, D. Kim, H.J. Kim, J. Kim, K. Char, C.T. Yavuz, J.W. Choi, Chem. Mater. **31**, 7910 (2019)
30. S.H. Je, T.H. Hwang, S.N. Talapaneni, O. Buyukcakir, H.J. Kim, J.S. Yu, S.G. Woo, M.C. Jang, B.K. Son, A. Coskun, J.W. Choi, ACS Energy Lett. **1**, 566 (2016)
31. Z.Y. Zhao, G.R. Li, Z. Wang, M. Feng, M.Z. Sun, X.X. Xue, R.P. Liu, H.S. Jia, Z.Z. Wang, W. Zhang, H.B. Li, Z.W. Chen, J. Power. Sources **434**, 226729 (2019)
32. F. Zhou, Z.S. Qiao, Y.G. Zhang, W.J. Xu, H.F. Zheng, Q.S. Xie, Q. Luo, L.S. Wang, B.H. Qu, D.L. Peng, Electrochim. Acta **349**, 136378 (2020)
33. E.V. Kuzmina, E.V. Karaseva, D.V. Kolosnitsyn, L.V. Sheina, N.V. Shakirova, V.S. Kolosnitsyn, J. Power. Sources **400**, 511 (2018)
34. A. Raulo, S. Bandyopadhyay, S. Ahamad, A. Gupta, R. Srivastava, P. Formanek, B. Nandan, J. Power. Sources **431**, 250 (2019)
35. W. Li, J. Hicks-Garner, J. Wang, J. Liu, A.F. Gross, E. Sherman, J. Graetz, J.J. Vajo, P. Liu, Chem. Mater. **26**, 3403 (2014)
36. K. Kim, P.J. Kim, J.P. Youngblood, V.G. Pol, Chemsuschem **11**, 2375 (2018)
37. A.A. Razzaq, Y.Z. Yao, R. Shah, P.W. Qi, L.X. Miao, M.Z. Chen, X.H. Zhao, Y. Peng, Z. Deng, Energy Storage Mater. **16**, 194 (2019)
38. S.J. Dai, Y. Feng, P. Wang, H. Wang, H.G. Liang, R.F. Wang, V. Linkov, S. Ji, Electrochim. Acta **321**, 134678 (2019)
39. H. Ye, Y. Li, Nano Res. Energy **1**, e9120012 (2022)
40. C.M. Li, H. Zhang, L. Otaegui, G. Singh, M. Armand, L.M. Rodriguez-Martinez, J. Power. Sources **326**, 1 (2016)
41. C. Yang, P. Li, J. Yu, L.D. Zhao, L. Kong, Energy **201**, 117718 (2020)
42. M. Cuisinier, C. Hart, M. Balasubramanian, A. Garsuch, L.F. Nazar, Adv. Energy Mater. **5**, 1401801 (2015)
43. B.S. Kim, S.M. Park, J. Electrochem. Soc. **140**, 115 (1993)
44. H.L. Pan, X.L. Wei, W.A. Henderson, Y.Y. Shao, J.Z. Chen, P. Bhattacharya, J. Xiao, J. Liu, Adv. Energy Mater. **5**, 1500113 (2015)
45. A. Gupta, A. Bhargav, A. Manthiram, Adv. Energy Mater. **9**, 1803096 (2019)
46. G. Zhang, H.J. Peng, C.Z. Zhao, X. Chen, L.D. Zhao, P. Li, J.Q. Huang, Q. Zhang, Angew. Chem. Int. Ed. **57**, 16732 (2018)
47. Q. Cheng, W. Xu, S. Qin, S. Das, T. Jin, A. Li, A.C. Li, B. Qie, P. Yao, H. Zhai, C. Shi, X. Yong, Y. Yang, Angew. Chem. Int. Ed. **58**, 5557 (2019)
48. T. Chivers, I. Drummond, Inorg. Chem. **11**, 2525 (1972)
49. R.P. Martin, W.H. Doub, J.L. Roberts, D.T. Sawyer, Inorg. Chem. **12**, 1921 (1973)
50. Tobishima, S. I., Yamamoto, H. and Matsuda, M., *Electrochim. Acta*, (1997).
51. Y.C. Lu, Q. He, H.A. Gasteiger, J. Phys. Chem. C **118**, 5733 (2014)
52. T. Fujinaga, T. Kuwamoto, S. Okazaki, M. Hojo, Bull. Chem. Soc. Japan **53**, 2851 (1980)
53. P. Leghié, J.-P. Lelieur, E. Levillain, Electrochem. Commun. **4**, 406 (2002)
54. J. Badoz-Lambling, R. Bonnaterre, G. Cauquis, M. Delamar, G. Demange, Electrochim. Acta **21**, 119 (1976)
55. R. Bonnaterre, G.J. Cauquis, Chem. Soc. Chem. Commun. **5**, 293 (1972)
56. A.S. Baranski, W.R. Fawcett, C.M. Gilbert, Anal. Chem. **57**, 166 (1985)
57. Y. Gorlin, A. Siebel, M. Piana, T. Huthwelker, H. Jha, G. Monsch, F. Kraus, H.A. Gasteiger, M. Tromp, J. Electrochem. Soc. **162**, A1146 (2015)
58. R. Chen, T. Zhao, J. Lu, F. Wu, L. Li, J. Chen, G. Tan, Y. Ye, K. Amine, Nano Lett. **13**, 4642 (2013)
59. P.G. Bruce, S.A. Freunberger, L.J. Hardwick, J.M. Tarascon, Nat. Mater. **11**, 19 (2011)
60. L. Suo, Y.S. Hu, H. Li, M. Armand, L. Chen, Nat. Commun. **4**, 1481 (2013)
61. F. Wu, J.Z. Chen, R.J. Chen, S.X. Wu, L. Li, S. Chen, T. Zhao, J. Phys. Chem. C **115**, 6057 (2011)
62. J. Paris, V. Plichon, Electrochim. Acta **26**, 1823 (1981)
63. Q. Zou, Y.C. Lu, J. Phys. Chem. Lett. **7**, 1518 (2016)
64. F.Y. Fan, W.C. Carter, Y.M. Chiang, Adv. Mater. **27**, 5203 (2015)
65. H.L. Pan, J.Z. Chen, R.G. Cao, V. Murugesan, N.N. Rajput, K.S. Han, K. Persson, L. Estevez, M.H. Engelhard, J.G. Zhang, K.T. Mueller, Y. Cui, Y.Y. Shao, J. Liu, Nat. Energy **2**, 813 (2017)
66. Z. Li, Y. Zhou, Y. Wang, Y.-C. Lu, Adv. Energy Mater. **9**, 1802207 (2019)
67. H. Chu, H. Noh, Y.-J. Kim, S. Yuk, J.-H. Lee, J. Lee, H. Kwack, Y. Kim, D.-K. Yang, H.-T. Kim, Nat. Commun. **10**, 188 (2019)
68. H. Chu, J. Jung, H. Noh, S. Yuk, J. Lee, J.-H. Lee, J. Baek, Y. Roh, H. Kwon, D.W. Choi, K. Sohn, Y.K. Kim, H.-T. Kim, Adv. Energy Mater. **10**, 2000493 (2020)
69. J. Jung, H. Chu, I. Kim, D.H. Lee, G. Doo, H. Kwon, W. Jo, S. Kim, H. Cho, H.-T. Kim, Adv. Sci. **10**, 2301006 (2023)
70. B. Celine, L. Jeam-Claude, P. Sébastien, A. Fannie, Electrochim. Acta **89**, 737 (2013)